Large-eddy simulation of separated flow over a swept wing with approximate near-wall modelling

N. Li and M. A. Leschziner
Imperial College
London, UK

ABSRACT

The paper investigates, by means of a simulation methodology, the flow separating from a 40 degrees backward-swept wing at 9 degrees incidence and Reynolds number of 210,000, based on the wing-root chord length. The Simulation corresponds to LDA, PIV and suction-side-topology measurements for the same geometry, conducted by other investigators specifically to provide validation data. The finest block-structured mesh contains 23·6 million nodes and is organised in 256 blocks to maximise mesh quality and facilitate parallel solution on multi-processor machines. The near-wall layer is resolved, to a thickness of about $y^+ = 20$, by means of parabolised URANS equations that include an algebraic eddy-viscosity model and from which the wall-shear stress is extracted to provide an unsteady boundary condition for the simulation. The numerical solution is in good agreement with the experimental behaviour over the 50-70% inboard portion of the span, but the simulation fails to resolve some complex features close to the wing tip, due to a premature leading-edge vortex breakdown and loss in vortex coherence. The comparisons and their discussion provide useful insight into various physical characteristics of this complex separated wing flow.

1.0 INTRODUCTION

Moderate to high sweep is a feature of most modern aircraft, especially of military planes. When the wing is thin, with high leading-edge curvature, even modest incidence can lead to separation, unless elaborate flow-control measures are taken. Depending on the sweep, different regimes of complex separation phenomena arise on the suction side. At low sweep, the flow can exhibit some characteristics akin to 'closed' (bubble) separation, observed in two-dimensional geometries. At high sweep, separation is of the 'open' (vortex) type, characterised by multiple vortical structures and separation and reattachment lines on the suction side. The boundary between the two regimes is not distinct, however. At the line of separation, the flow may or may not be turbulent. Contamination from the spanwise motion favours transition on attachment, but close to the wing root (or apex) transition may occur in the separated shear layer. In the case of vortex separation, the flow above the wing is highly swirling and the vortex contains a core that moves at high speed in the axial direction. The body forces associated with the swirl can make the vortex super-critical, strongly damp turbulence and hence reduce the spreading rate of the vortex. Secondary separation zones also arise on the wing, adding to the

Paper No. 3172. This is an invited paper published to celebrate the 100th anniversary of Imperial College, London.

https://doi.org/10.1017/S0001924000004863 Published online by Cambridge University Press

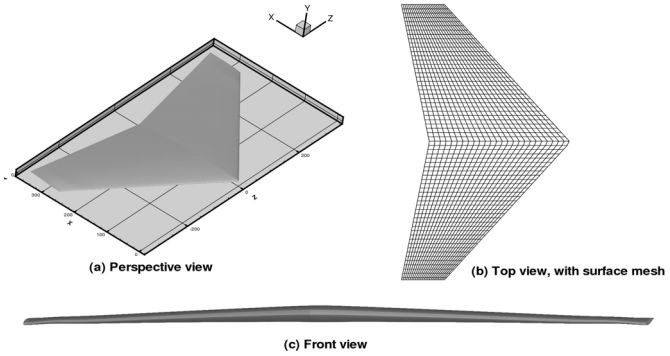


Figure 1. Geometry of the swept wing under consideration.

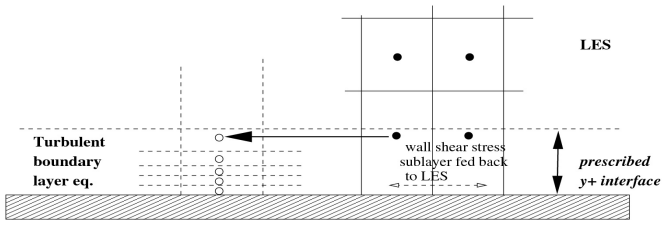


Figure 2. Schematic of the two-layer zonal scheme.

complexity of the flow and creating highly challenging conditions for both experiment and numerical prediction.

RANS models, although performing reasonably well in relatively simple attached conditions, tend to display a high degree of predictive variability and serious defects in complex three-dimensional separation. LES, on the other hand, is well suited to such flows, but is costly, requires very high mesh quality, and demands the use of minimally diffusive numerical schemes that have low levels of robustness. More seriously, when the flow to be simulated is sensitive to the frictional characteristics at bounding walls – as is often the case in external aerodynamics – pure LES faces formidable near-wall-resolution challenges, with the mesh density having to be increased roughly in proportion to Re^2. At present, these challenges can only be addressed by the use of hybrid or zonal LES-RANS method, which combine some type of URANS near-wall strategy with an outer LES solution.

Computational studies of separation from highly-swept wings, with emphasis on fundamental flow features and turbulence, are rare. Most studies are directed towards clean delta wings and assume sharp-leading-edge separation[1-3]. The LES study by Mary[3] demonstrates, in particular, a substantial sensitivity of the predicted flow above the suction side to the near-wall treatment within one and the same LES strategy. There is also a numerical study of the development and transition of a three-dimensional boundary layer on a swept wing with its curvature neglected and its span assumed to be infinite[4]. These flow conditions, although very complex, are considerably simpler than those around the present wing, with its highly curved leading edge and twisted geometry. At present, there are no theoretical models capable of predicting such separation with any degree of reliability, nor can the nature of the intricate response of the separation characteristics to sweep and angle of attack be convincingly explained.

This paper reports the application of a 'zonal' LES method, incorporating an approximate RANS-based near-wall treatment, to the separated flow around a swept wing at moderate incidence for which experimental data have been generated specifically for the purpose of examining the predictive capabilities of alternative computational strategies when applied to highly-swept wings.

2.0 THE GEOMETRY

The geometry considered is shown in Fig. 1. This is a fixed, clean wing with a 40-degree sweep angle, highly-curved leading edge, sharp trailing edge, rounded tips, twisted shape and a maximum thickness of 6% of the root-chord length. An aluminium model, of span of about 0·65 meter, was specially manufactured for wind-tunnel testing at the University of Manchester, UK (Zhang *et al*[5]). The experimental Reynolds number is 210,000, based on the root-chord length and the free-stream velocity. The experimental programme included flow visualisations, surface pressure measurements and extensive three-dimensional LDA/PIV traverses to map the velocity and turbulence fields. There are also measurements at a much higher Reynolds number that is, at present, beyond the capability of current numerical simulation. At the time of writing, a substantial proportion of the experimental data has yet to be published, and only a limited range of the data can be used herein to assess the simulation.

3.0 THE COMPUTATIONAL APPROACH

The computational method rests on a general multi-block, collocated-storage finite-volume scheme with non-orthogonal-mesh capabilities, allowing the mesh to be body-fitted. The scheme is second-order accurate in space, utilising central differencing for advection and diffusion. Time marching is based on a fractional-step method, with the time derivative being discretised by a second-order backward-biased approximation. The flux terms are advanced explicitly with the Adams-Bashforth method. The provisional velocity field is then corrected via the pressure gradient by a projection onto a divergence-free velocity field. To this end, the pressure is computed as a solution to the pressure-Poisson problem by means of a three-dimensional V-cycle multigrid algorithm operating in conjunction with a successive line over-relaxation scheme. The code is fully parallelised using MPI and was run on several multi-processor computers with up to 256 processors. The procedure is more fully described in Temmerman *et al*[6]. Subgrid stresses are approximated with the dynamic Smagorinsky model of Germano[7].

For the complex geometry and the high Reynolds number under consideration, the computational resources required to fully resolve the near-wall structure are beyond the range considered acceptable in a practical environment: the estimated mesh density required to achieve full near-wall resolution is around 300 million nodes. In contrast, the results presented below have been obtained with a mesh containing only around 24 million nodes. With this mesh, described later in more detail, the time-averaged, universal wall-normal distance of the wall-nearest nodes, y^+, calculated using the mean local friction velocity, is less than 20 over most of the surface, but reaches 40 in some isolated highly-shear near-wall regions. This necessitates the use of a special near-wall-modelling strategy, as the simple application of a no-slip condition would result in a grossly erroneous representation of frictional wall effects. The approach taken here is to use a two-layer zonal method, the main characteristics of which are conveyed in Fig. 2. Its details are documented in Tessicini *et al*[8]. In its most general implementation, the near-wall flow is modelled by the following parabolised Navier-Stokes equations:

$$\underbrace{\frac{\partial \rho \tilde{U}_i}{\partial t} + \frac{\partial \rho \tilde{U}_i \tilde{U}_j}{\partial x_j} + \frac{\partial \tilde{P}}{\partial x_i}}_{F_i} = \frac{\partial}{\partial y}\left[\left(\mu + \mu_t\right)\frac{\partial \tilde{U}_i}{\partial y}\right] \qquad i = 1,3 \qquad \ldots (1)$$

https://doi.org/10.1017/S0001924000004863 Published online by Cambridge University Press

where y denotes the direction normal to the wall and i identifies the wall-parallel directions (1 and 3). The equations are solved on a sub-layer grid embedded into the global LES mesh. The left-hand-side terms in F_i in Equation (1) can be included selectively to achieve different degrees of simplification of the full model. The economy of the scheme derives from the fact that the pressure field, evaluated on the wall-nearest layer of the LES mesh, is imposed on the parabolised near-wall-layer equations and does not need to be calculated in that layer. In the present application, the convection and pressure terms have been excluded. This simplification was also adopted by Tessicini *et al*[9] in a recent study of three-dimensional separation from curved surfaces at a Reynolds number similar to that of the present configuration, and was demonstrated to give satisfactory results. The inclusion of convection requires a full three-dimension storage and solution in the near-wall layer, thus resulting in a major increase in computational cost. Moreover, as shown in Leschziner *et al*[10], this inclusion does not offer advantages in channel-flow simulations.

In the present implementation, the eddy viscosity μ_t in Equation (1) was derived from a mixing-length-type turbulence model with appropriate van Driest near-wall damping. This simple approach may be justified by the argument that the outcome of the inner-layer solution, effected over a very thin region, is merely the provision of realistic values for the wall shear stress, which then serves as a wall boundary condition for the LES domain. There is considerable uncertainty, in general, about the adequacy of RANS closures in highly unsteady conditions, and the use of elaborate closures for the stated purpose is judged to be unjustified. Temmerman *et al*[6,11] discuss the issue of modelling level and dynamic model adjustment within a hybrid LES-RANS strategy, but in their case, the unsteady-flow solution within the near-wall layer is fully integrated into the LES solution outside the layer, and is thus part and parcel of the simulation as a whole. The present approach is quite different in nature, and may be regarded (with convection omitted) as an elaborate wall-function method. Successful applications of this method range from simple channel flow to complex three-dimensional flows separating from a hill-shaped obstruction in a duct (Tessicini *et al*[9]). The latter case is especially pertinent to the present application, for it involves a complex three-dimensional separation from the curved surface of a body subjected to a turbulent boundary layer at a Reynolds number similar to the present value.

Because LES requires a high mesh quality, much attention was devoted to its generation, with the added requirement of a load-balanced parallel execution being taken into account. The end result is the H-topology multi-block mesh, shown in Fig. 3. At its forward and outer boundaries, the experimental free-stream velocity is prescribed, while convective outflow conditions are used at the rear boundary. Justification for the simple approach adopted at the outer boundary had been provided by specific experimental measurements, preceding the definition of the mesh and verifying the existence of constant-velocity, low-turbulence conditions at a distance of one full span beyond the wing tips. Close to the wall, much care was exercised to ensure appropriately low levels of cell-aspect ratio, skewness and expansion ratio of the LES mesh. These efforts were decisively facilitated by the use of the zonal strategy, which permitted the first grid node to be placed outside the viscous sublayer. A preliminary study using 7·5 million nodes was first conducted and this was followed by detailed studies on the much finer mesh of 23·6 million cells (384 × 192 × 320). The mesh has an especially high density around the leading edge, trailing edge and wing tips, and the maximum cell aspect ratio of the mesh, at the wall, is about 70. The mesh was partitioned into 256 equal-sized blocks for efficient parallel computing, as is shown in the upper-right plot of Fig. 3.

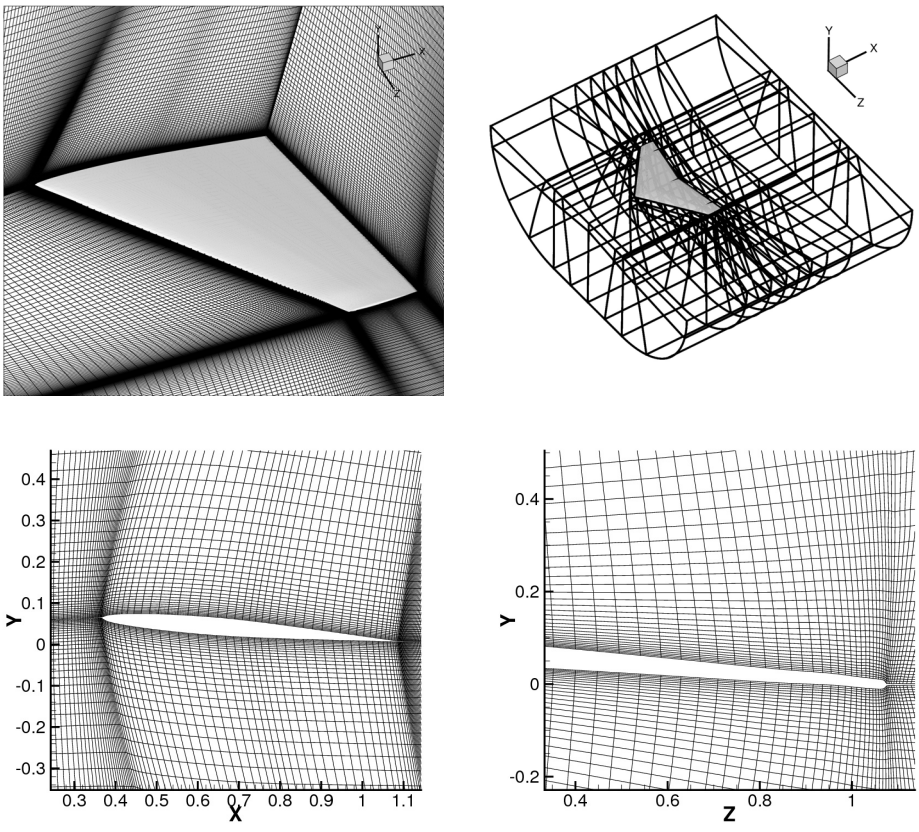


Figure 3. Upper-left: numerical mesh close to the wing. Upper-right: block partitions for the computational domain (bottom half only); lower-left: mesh across 50% wing-span plane; lower-right: span-wise cross-section of the mesh.

https://doi.org/10.1017/S0001924000004863 Published online by Cambridge University Press

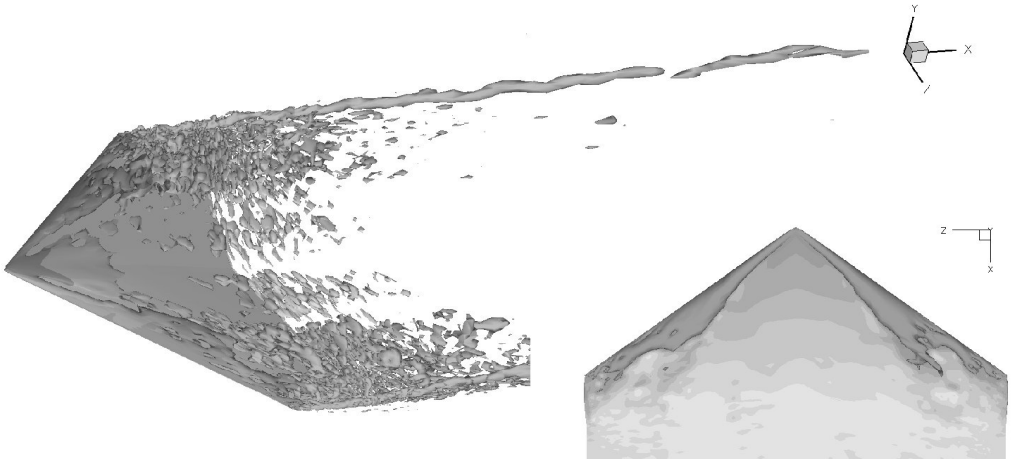


Figure 4. Coherent structures above and behind the wing, identified by the Q-criterion and by iso-surfaces of pressure, to highlight the vortical structures above the wing.

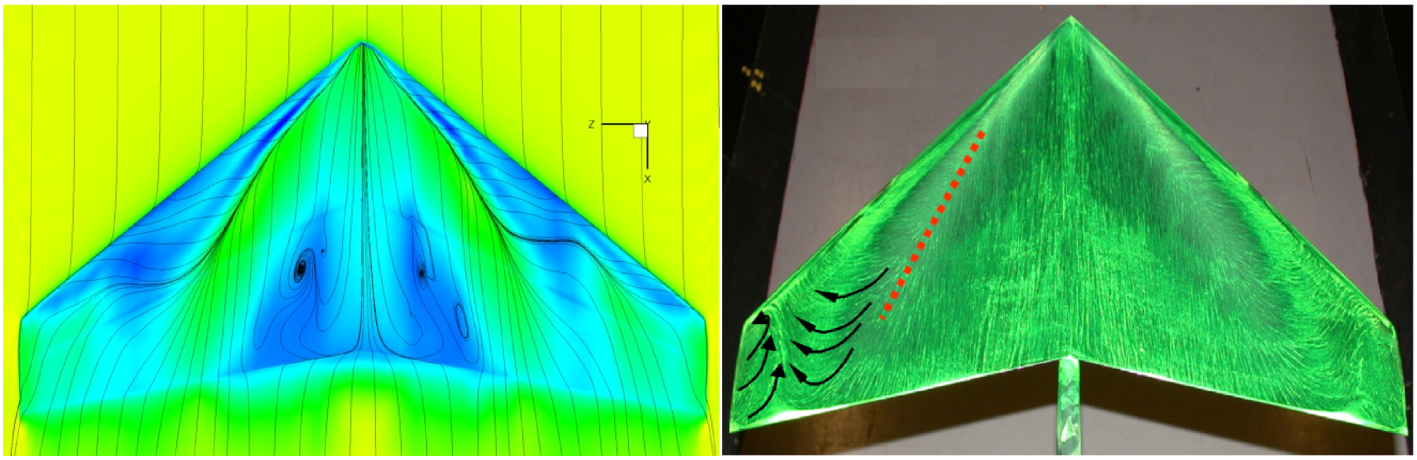


Figure 5. Surface streak-line pattern on the suction side. Left: predicted by the simulation. Right: oil-film flow visualisation.

The simulations reported herein covered a period equivalent to seven flow-through times, of which five were used to obtain statistical data. A run with the fine grid required around 30,000 IBM POWER5 CPU hours on the HPCx facility, the most powerful machine available to the academic community in the UK. A period of five through-times is rather short, but resource limitations dictated economy. As will be shown below, the dominant features in this flow are strong leading-edge vortices. These largest-scale features are relatively stable and the flow can therefore be expected not to require the long integration periods needed, for example, for bluff-body separation involving periodic shedding of large structures.

5.0 RESULTS AND DISCUSSIONS

Results are presented here for an angle of attack (AoA) of 9 degrees, including an effective AoA increment due to the twisted shape of the wing itself. The flow at this AoA is of particular interest, because it is clearly seen to be separated and contains various complex vortical structures.

An overall view of the flow is conveyed by Figs 4-7. Figure 4 provides an instantaneous view of the unsteady flow by means of iso-surfaces of pressure and the so-called 'Q-criterion', defined as $Q = 0{\cdot}5\ (\Omega_{ij}\Omega_{ij} - S_{ij}S_{ij})$, where Ω is the vorticity tensor and S is the strain tensor. This second-order velocity-gradient invariant can be shown to be the divergence of the acceleration vector. The visualisation of constant-value surfaces of both Q and pressure bring out, preferentially, coherent vortical structures. Close to the leading edges, both sets of iso-surfaces indicated that the flow is dominated by well-formed leading-edge vortices, which display coherence over a substantial part of the leading edge. The Q-surfaces show, however, that these vortices become highly turbulent within a distance of approximately 10-20% of chord, especially over the outer portions of the wing in which the leading-edge vortices are no longer recognisable as coherent features. Also brought out well in Fig. 4 are the cores of the strong wing-tip vortices in the wake.

Figure 5 gives a comparison between computed surface streak lines and an experimental oil-film visualisation on the suction side. This comparison shows some major common features, but also important differences, reflected in profiles to follow. A major common feature is the well-defined attachment line emanating from the apex and extending towards the trailing edge at an angle of approximately 25 degrees relative to the leading edge. This line has been inserted into the experimental plot as a series of dots. The well-defined computed attachment line has a slightly lower angle, and is shorter, but appears otherwise to be close to its experimental counterpart. The latter difference may be rooted in the early vortex breakdown and the intense turbulent mixing seen

https://doi.org/10.1017/S0001924000004863 Published online by Cambridge University Press

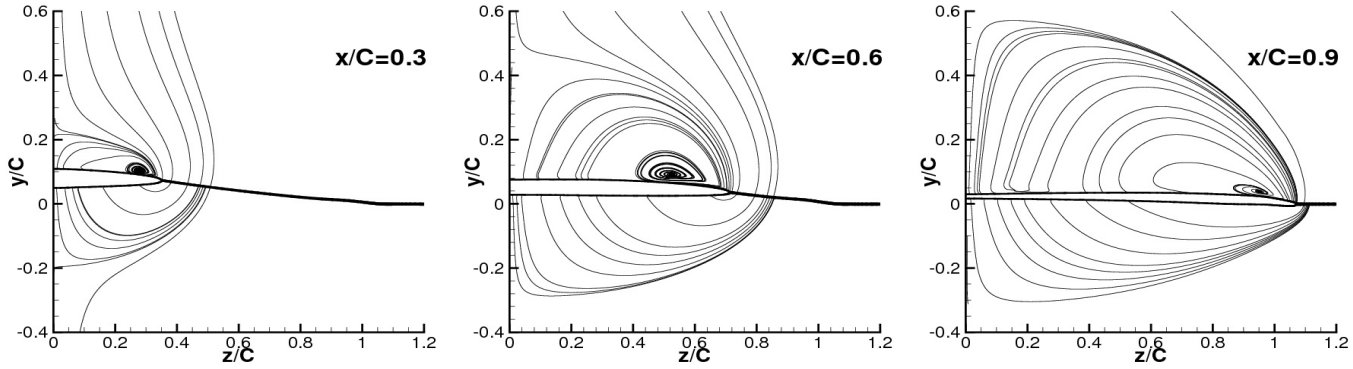


Figure 6. Streakline patterns constructed from the transverse- (swirl-)velocity components at various streamwise cross-sections.

in the Q-plot in Fig. 4 beyond 70% of span. This supposition is reinforced by the computational streak-line plots at three transverse planes, shown in Fig. 6. Up to $x/C = 0{\cdot}6$, the leading-edge vortex is tight and well defined, but at $x/C = 0{\cdot}9$ it is much weaker and more diffuse, indicating some major change in state between these two locations.

A closer examination of the surface streaks shows a number of more important differences. The experimental view indicated that the near-wall flow in the central portion of the wing, within the wedge defined by the attachment lines, is characterised by a simple forward motion from the leading edge to the trailing edge. This is reproduced by the computations over most of the area, except for two weak vortical separation regions predicted in the central rear portion of the wing in which turbulence is very weak. More important differences arise in the wing-tip regions. As indicated by arrows inserted by the writers into the oil-flow photograph, the near-wall flow ahead of the attachment line is progressively turning backwards towards the leading edge beyond 70% of the span. This behaviour is also captured by the computation, although the degree of turning is lower and the extent of the region involved smaller. At around 90% of span, the experimental view reveals the existence of a secondary separation line that is formed by fluid over the wing moving outwards, as described above, and wing-tip fluid moving inwards and towards the leading edge, as indicated by the arrows inserted into the experimental photograph. The two streams thus 'collide' and detach to merge into the wing-tip vortex. This feature is not resolved by the simulation, and the consequence is, as will be shown below, that the predicted displacement in this region is seriously under-estimated.

Figure 7 shows the locus of the core of the leading-edge vortex as it evolves over the suction side. Both the simulation and the experiment show that the vortex grows in size as it progresses downstream, and the distance of the core to the wing surface also grows (roughly linearly). However, the predicted core path is somewhat further away from the suction side. In the experiment, the vortex core begins to turn rapidly away from the surface at around 70% of the span, while the vortex remains stable, this upward turn being accompanied by the rapid turning of the surface flow towards the leading edge and a deceleration effected by the interaction with the wing-tip separation region. In contrast, and again, in agreement with earlier interpretations, the simulation suggests that the vortex become unstable around this location and undergoes a breakdown process, after which the coherence and integrity of the vortex is lost. This drastic change in the vortex behaviour is reflected by the sudden outward turn in the separation line shown in Fig. 5. As noted earlier, the oil-flow image in the same figure shows similar outward turning, but further downstream than predicted by the simulation.

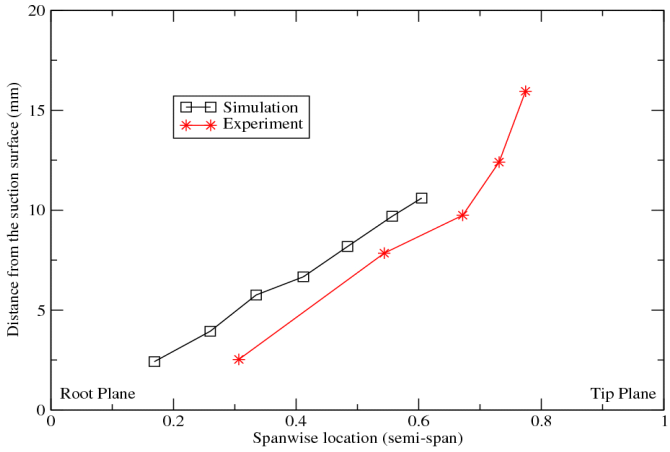


Figure 7. Locus of the core of the leading-edge vortex.

A detailed comparison of the experimental and simulated flow is made possible by the availability of LDA data[5] for the velocity over the suction side of the wing. Such comparisons for surface-normal profiles of streamwise and spanwise velocity components are given in Fig. 8 for the spanwise stations $z/L_s = 0{\cdot}1$, $0{\cdot}3$, $0{\cdot}5$, $0{\cdot}7$ and $0{\cdot}9$, respectively, where L_s represents the half-wing span. For each spanwise station, comparisons are given at five chordwise positions, ranging from 10% to 90% along the local chord line. The comparisons show fairly good agreement in the first two spanwise locations. One notable exception relates to the chordwise rear locations after 70% of chord at $z/L_s = 0{\cdot}3$. As pointed out earlier in the discussion of the overall flow features, the simulation returns weak reverse-flow regions in the central rear portion of the wing, in contrast to the attached conditions measured. This is confirmed by the streamwise velocity profiles at 70% and 90% of chord, which indicate a thicker near-wall layer and a weak reverse flow at the latter station. The spanwise motion in the rear part of the leading-edge vortex (30% of chord) is too weak, and this goes hand-in-hand with the chord-wise shorter leading-edge vortex predicted. At $z/L_s = 0{\cdot}5$, agreement is pleasingly close in most respects, except, again, for an indication that the leading-edge vortex has a slightly lower streamwise extent than that measured. The U-velocity profiles are seen to feature inflexion points and indicate deceleration and thickening of the near-wall layer, associated with the attachment (impingement) process along the line shown in Fig. 5.

https://doi.org/10.1017/S0001924000004863 Published online by Cambridge University Press

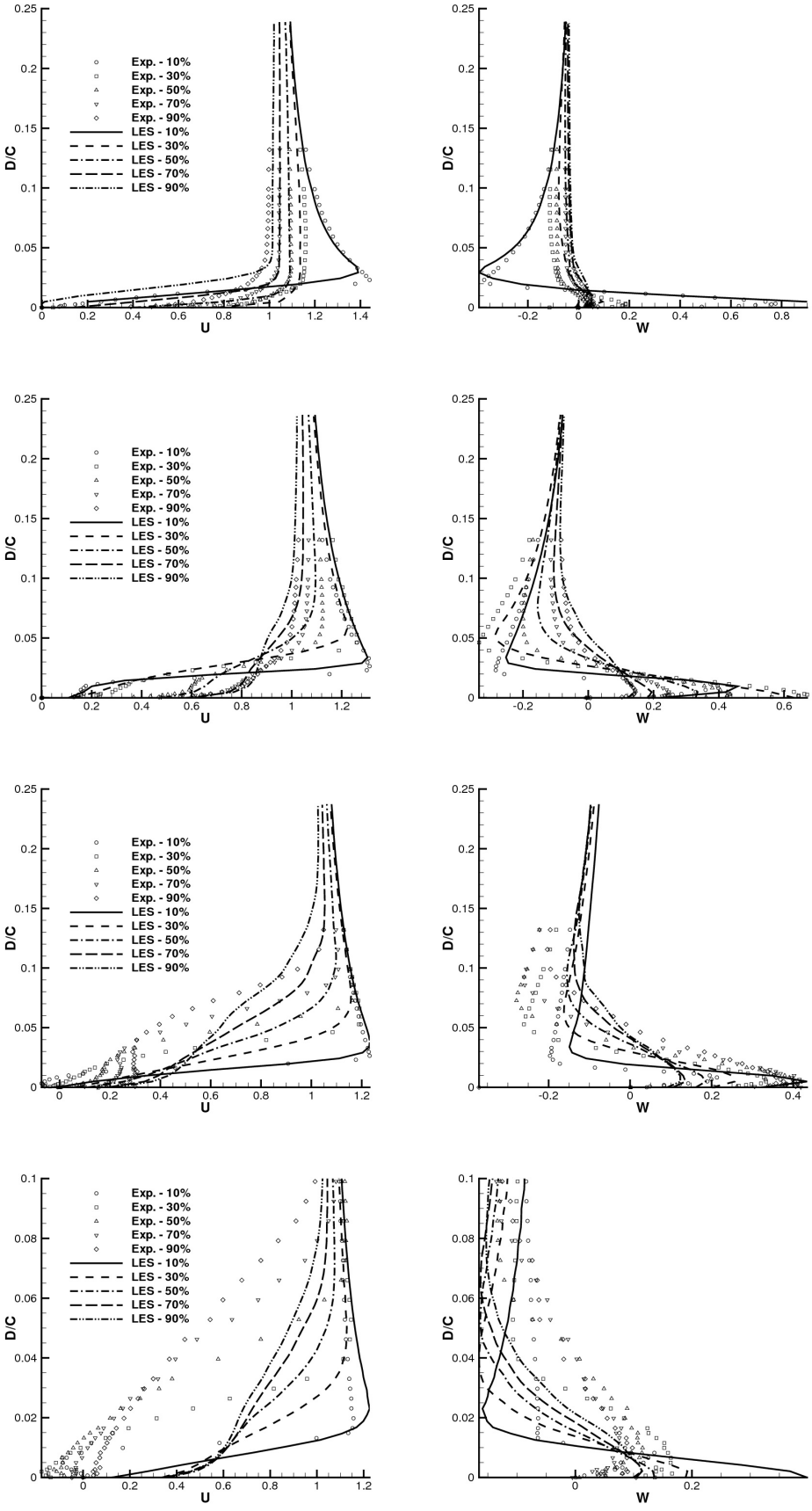


Figure 8. Velocity profiles on various wing-span planes. From top to the bottom: 30%, 50%, 70%, 90% wing-span. Left: streamwise component; right: spanwise component.

https://doi.org/10.1017/S0001924000004863 Published online by Cambridge University Press

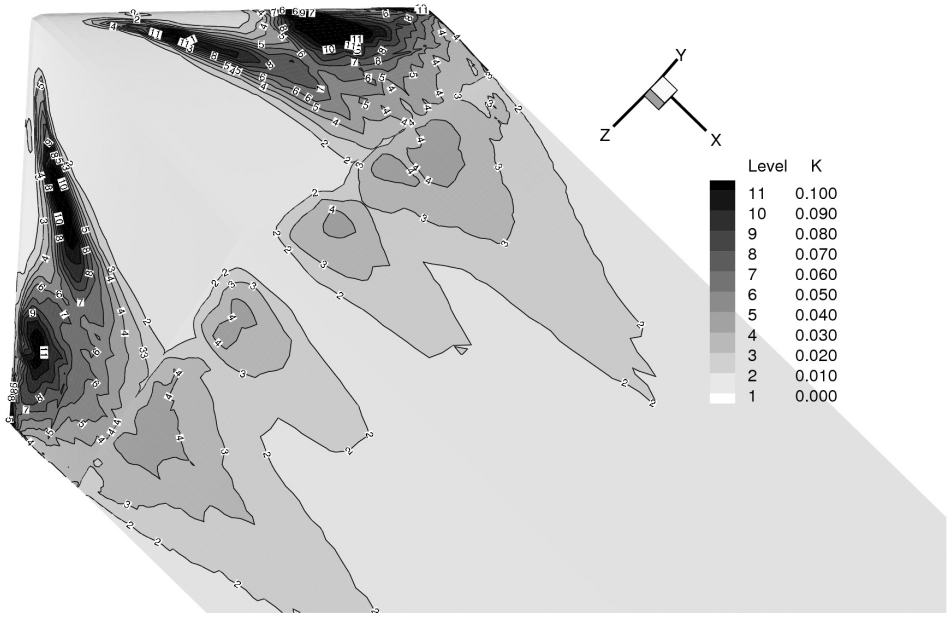


Figure 9. Turbulence energy distribution above the wing and in the wakes.

A less favourable picture presents itself in the comparisons for z/L_s = 0·7 and especially 0·9. The experiments indicate a rapid thickening of the near-wall layer and a wall-normal outward shift of the leading-edge vortex. The latter is consistent with comments made in relation to Fig. 7, while the former reflects the rapid turning of the flow towards the leading edge and the interaction of the flow in this region with the wing-tip separation. The simulation underestimates both features. The computed flow turns at a significantly lower rate, so that the thickening of the near-wall layer is hindered. At the same time, the intensity of the leading-edge vortex is much diminished, and this is entirely consistent with earlier interpretations of the vortex breakdown, which appears to take place at around z/L_s = 0·7, thus leading to the intense turbulence and mixing indicated in Fig. 4. At z/L_s = 0·9, there are clearly major discrepancies between the experiment and the simulation. As is recognised from the experimental W-profiles, this position is marginally inboard of the separation line, indicated by the bright band close to the wing tip in Fig. 5. At this position, the experimental flow is characterised by a very thick near-wall layer with reverse flow due to the interaction of the inboard motion associated with the wing-tip separation and the general outboard motion. As pointed out earlier, this process is not resolved by the simulation, which predicts a rear-ward motion of the wing-tip vortex and thus a much thinner near-wall layer. At this position, the spanwise motion is relatively weak (see also Fig. 6) and also confined to the near-wall region, because of the insufficient wall-normal displacement. The origin of these discrepancies is uncertain at this time, but is likely to be rooted to a considerable extent in insufficient resolution in the wing-tip area. The only route to confirming this supposition is to perform simulations with the grid density at least doubled over the outboard 50% of the half-span. This would push the grid size to around 100 million nodes, which exemplifies the challenges of applying LES to non-bluff-body external flows of the present ilk.

Results for the turbulence field are given in Figs 9 to 11. The former provides a view of the turbulence energy, k/U_∞^2 , across the grid plane closest to the suction surface, namely y^+ of the order 20. Over the central portion of the wing, turbulence is very low, and this will also be demonstrated by turbulence-energy profiles to follow. Close to the leading edge, within a spanwise position extending from around 25% and 65% span, there are clear indications that the flow is laminar, undergoing transition at around 5-10% of chord. This is also suggested by the oil-film photograph, where the laminar region is identified by dark strips somewhat closer to the leading edge than suggested by the simulation. The turbulence level is highest in two areas: around the attachment line, where highly turbulent fluid from the leading-edge vortex impinges on the wing surface, and close to the wing tip, where, as seen from Figs 4 and 5, highly turbulent fluid from the vortex, following its breakdown, is transported across the suction side towards the leading edge and wing tip. The wake behind the wing is also seen to be highly turbulent, due to a combination of convective transport of turbulence from upstream and the instability and transition to turbulence in the sheared wake behind the trailing edge.

Profiles of turbulence energy, at the same positions as those to which velocity profiles relate, are given in Fig. 10. At 30% span, the flow is essentially non-turbulent over most of the chord, except for the position closest to the leading edge, where the detached leading-edge vortex is past transition and highly turbulent. At 50% span, the experiments suggest that transition is essentially complete well before 10% of chord, at which location the turbulence energy is extremely high. The entire flow over the suction side at this spanwise location is then turbulent, with the measured level of turbulence diminishing gradually. This latter trend is also exhibited by the simulation, except for the major difference at 10% at which the simulation suggests later transition. This is confirmed by Fig. 11, which shows computed contours of turbulence energy across the same spanwise location. The maximum turbulence level is evidently reached around 25% of chord (at x/C = 0·62), and the presence of a relatively broad low-turbulence strip in the leading-edge region, noted earlier by reference to Fig. 10, is consistent with this result. The delayed transition aside, it may be said that the representation of the turbulence state at 50% span is encouraging. In line with the mean-velocity field, agreement is less good at 70% and poor at 90%. As noted earlier, the simulation suggests a major breakdown of the vortex around this position, with a loss of vortex integrity. While the velocity profiles in Fig. 8 provides no clear indication of such a breakdown – the predicted thickness of the near-wall layer is considerably lower than the experimental value – the computed turbulence-energy profile provides clear pointers to this break-down through the substantially higher level of turbulence predicted relative to that measured. The excess in the computed level is particularly pronounced close to the wall, and it is entirely plausible that this

https://doi.org/10.1017/S0001924000004863 Published online by Cambridge University Press

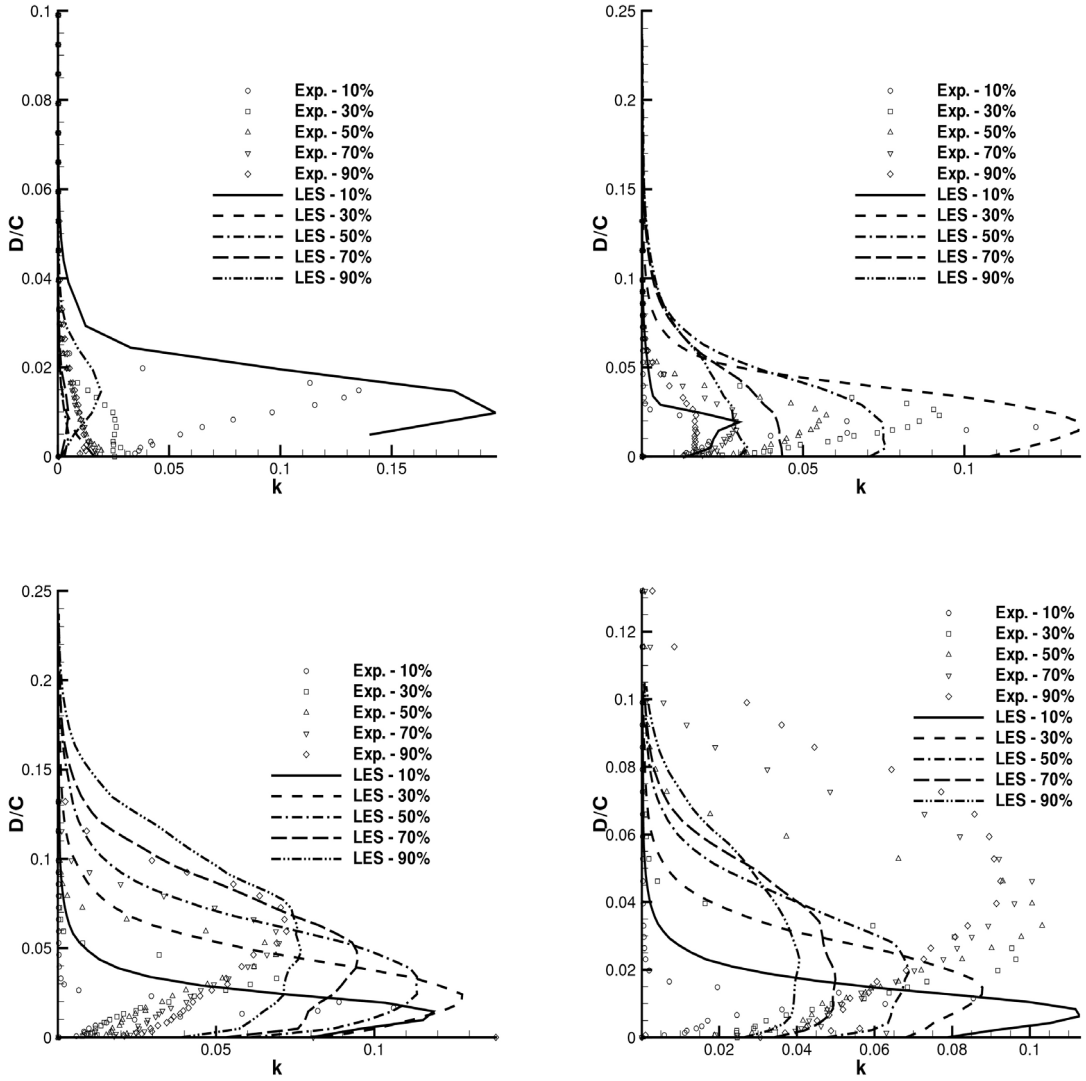


Figure 10. Turbulent energy profiles on various wing-span planes. Upper-left: 30% wing-span; upper-right: 50% wing-span; lower-left: 70% wing-span; lower-right: 90% wing-span.

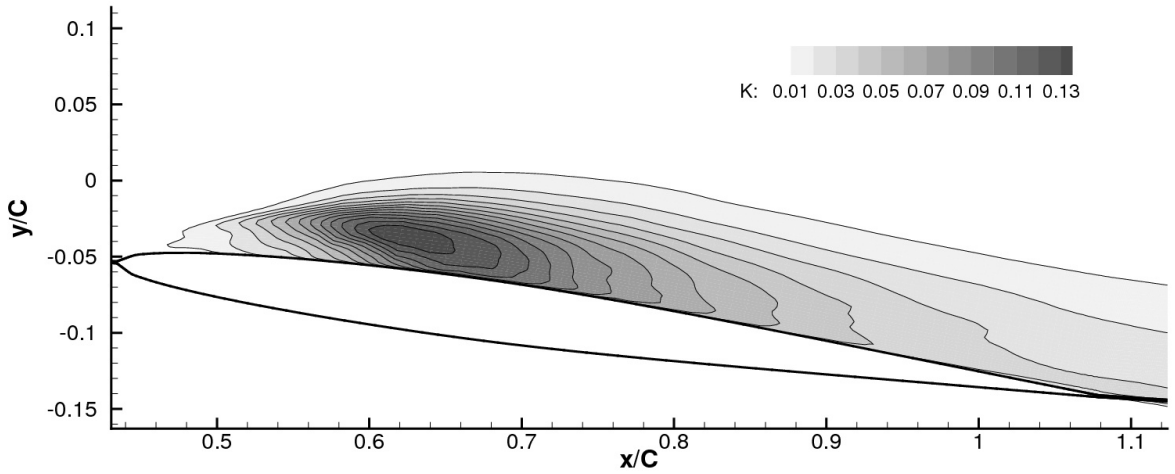


Figure 11. Turbulence energy contours across 50% wing span.

https://doi.org/10.1017/S0001924000004863 Published online by Cambridge University Press

excess and the momentum mixing that goes with it are responsible for the inhibition of the trend towards separation that is clearly exhibited by the *U*-velocity profiles in Fig. 8. At 90% of span, the comparison of velocity profiles in Fig. 8 has earlier revealed that separation is suppressed in the simulation, and this is again directly linked to the vortex breakdown observed further inboard. While the level of turbulence in outer regions, away from the wing, is too low, due to the much lower displacement from the wing and lower shear strain in the outer region, the predicted near-wall turbulence level is again too high, and this goes hand-in-hand with the resistance to separation.

Thus, in summary, it is encouraging to observe that the general characteristics of the turbulence field are reproduced, at least qualitatively, despite the highly challenging nature of the flow and the compromises that had to be made in respect of resolution. The profiles of the turbulence energy are generally consistent with features of the velocity field. Importantly, the computed turbulence field provides evidence that the predicted vortex breakdown at around 70% of span is indeed the process that is mainly responsible for the poor agreement between the simulation and the experiment towards the wing tip.

5.0 CONCLUSIONS

The study provides, if nothing else, a good demonstration of the challenges involved in exploiting LES for highly complex external flows that combine large-scale separation with substantial attached regions in which wall friction has important effects on the flow. The comparisons presented contain a mixture of encouraging messages and warning signs. On the positive side, it may be claimed that all major flow and turbulence characteristics inboard of around 60% of the span have been represented well. In particular, the principal attachment line and the structure of the leading-edge vortex, as well as the locus of its centre, have been reproduced broadly correctly. Moreover, the transitional character of the flow detaching from the leading edge is returned, although transition appears delayed relative to the experiment, the latter suggesting transition to occur quickly after the vortex separates from the leading edge. On the negative side, the predictive fidelity of the simulation deteriorates seriously as the wing tip is approached. The simulation predicts, in contrast to the experiment, a rapid breakdown in the vortex beyond 70% of span, into a highly turbulent state, so that the vortex loses its coherence. One consequence of this breakdown is that the re-orientation of the near-wall flow within the vortex, from a predominantly span-wise direction towards the leading edge, is substantially underestimated. Two associated defects are, first, that the formation of an inboard-directed secondary flow from the tip is suppressed, and second, that the separation line formed by the collision of the primary outward flow and the secondary inward flow, at around 95% of chord, is not reproduced.

The origin of the defects identified above is currently a matter of speculation. It seems reasonable to assume, however, that a significantly higher resolution towards the wing tip would be beneficial, especially in the surface-parallel directions, in which case a mesh of around 100 million nodes may well be necessary, within the present H-topology, to represent the flow across the entire span satisfactorily. Even within this range of node density, wall-normal refinement very close to the wall, subject to maintaining a modest cell-aspect ratio, would not be possible to the extent of rendering the zonal approach superfluous. This approximate treatment may also have contributed to the defects observed. A more secure judgement can thus only arise from further studies with finer grids.

ACKNOWLEDGMENTS

The authors gratefully acknowledge the financial support provided by BAE Systems and EPSRC through the DARP project '*Highly Swept Leading Edge Separation*'. The authors are also grateful to Dr Shanying Zhang and Dr John Turner, University of Manchester, for making available information and data arising from the related experimental programme, but not fully published at the time of writing.

REFERENCES

1. GORDNIER, R.E. Computational study of a turbulent delta-wing flowfield using two-equation turbulence models, 1996, AIAA paper 96-2076.
2. RIZZETTA, D.P. Numerical simulation of the interaction between leading-edge vortex and vertical tail, *AIAA J*, 1997, **35**, pp 756-757.
3. MARY, I. Large eddy simulation of vortex breakdown behind a delta wing, *Int J Heat and Fluid Flow*, 2003, **24**, (4), pp 596-605.
4. HUAI, X., JOSLIN, R.D. and PIOMELLI, U. Large-eddy simulation of boundary layer transition on swept wings, Transition, turbulence and combustion; Proceedings of the Workshop, Hampton, VA, USA; Netherlands; 7 June-2 July 1993, pp 369-378.
5. ZHANG, S., JAWORSKI, A.J., TURNER, J. and WOOD, N.J. Separation and vortex generation in the flow over a highly swept wing, an experimental study based on three-component LDA measurement, to appear in *Aeronaut J*.
6. TEMMERMAN, L., LESCHZINER, M.A. and HANJALIĆ, K. A-priori studies of a near-wall RANS model within a hybrid LES/RANS scheme, *Engineering Turbulence Modelling and Experiments 5*. RODI, W. and FUEYO, N. (Eds), Elsevier, 2002, 317-326.
7. GERMANO, M., PIOMELLI, U., MOIN, P. and CABOT, W.H. A dynamic subgrid-scale eddy viscosity model, *Physics of Fluids A: Fluid Dynamics*, 1991, **3**, (7), pp 1760-1765.
8. TESSICINI, F., TEMMERMAN, L. and LESCHZINER, M.A. Approximate near-wall treatments based on zonal and hybrid RANSLES methods for LES at high Reynolds numbers, *Int J Heat and Fluid Flow*, 2006, **27**, (5), pp 789-799.
9. TESSICINI, F., LI, N. and LESCHZINER, M.A. Large-eddy simulation of three-dimensional flow around a hill-shaped obstruction with a zonal near-wall approximation, *Int J Heat and Fluid Flow*, 2007, **28**, (5), pp 894-908.
10. LESCHZINER, M.A., LI, N. and TESSICINI F. Computational methods combining LES with approximate wall-layer models for predicting separated turbulent near-wall flows, Wall Modelling in LES: Method Development and Application, ERCOFTAC Bulletin, **72**, 2007.
11. TEMMERMAN, L., HADZIABDIC, M., LESCHZINER, M.A. and HANJALIĆ, K. A hybrid two-layer URANS-LES approach for large eddy simulation at high Reynolds numbers, *Int J Heat and Fluid Flow*, 2004, **26**, (2), pp 173-190.

https://doi.org/10.1017/S0001924000004863 Published online by Cambridge University Press